Fluid particle dynamics and the non-local origin of the Reynolds shear stress

Peter S. Bernard[1,†] **and Martin A. Erinin**[1]

[1]Department of Mechanical Engineering, University of Maryland, College Park, MD 20742, USA

The causative factors leading to the Reynolds shear stress distribution in turbulent channel flow are analysed via a backward particle path analysis. It is found that the classical displacement transport mechanism, by which changes in the mean velocity field over a mixing time correlate with the wall-normal velocity, is the dominant source of Reynolds shear stress. Approximately 20 % of channel flow at any given time contains fluid motions that contribute to displacement transport. Much rarer events provide a small but non-negligible contribution to the Reynolds shear stress due to fluid particle accelerations and long-lived correlations deriving from structural features of the near-wall flow. The Reynolds shear stress in channel flow is shown to be a non-local phenomenon that is not conducive to description via a local model and particularly one depending directly on the local mean velocity gradient.

1. Introduction

The modelling of turbulent transport phenomena is a central aspect of methodologies for turbulent flow prediction, whether based on Reynolds-averaged Navier–Stokes (RANS) solutions or large eddy simulations (LES) (Bernard & Wallace 2002). The most widely used RANS models (Jones & Launder 1972; Menter 1994; Spalart & Allmaras 1994; Wilcox 2008) rely on a linear stress mean rate-of-strain transport model that mimics the physics underlying the linear constitutive law for the stress tensor in the Navier–Stokes equation. Nonlinear generalizations of linear models (Speziale 1987; Gatski & Speziale 1993) including algebraic Reynolds stress models recognize the inadequacies of the gradient transport formalism and seek to expand the range of physics to which the transport models can be applied. For LES, linear gradient models of the subgrid stresses are ubiquitous, so that most effort, as in the case of RANS, goes into deciding on the form of the subgrid-scale eddy viscosity (Lesieur & Métais 1996; Sagaut 2006) rather than developing new means of modelling transport physics. It is also the case that the dispersal of many scalar fields in turbulent flow such as energy and mass contaminants is most often modelled via the Reynolds analogy wherein the scalar flux is assumed to be proportional to the momentum flux (Kays & Crawford 1993; Araya & Castillo 2012). In practical terms, this almost

† Email address for correspondence: bernard@umd.edu

always means that gradient forms are used to model the scalar flux, wherein the eddy diffusivity is taken to be proportional to the eddy viscosity via the turbulent Prandtl or Schmidt number.

Knowledge of the physical processes leading to transport remains incomplete, so that turbulence prediction methods depending on modelled transport correlations are of limited accuracy. It is equally problematical that often what is known about transport is not readily incorporated into the development of useful formulae relevant to engineering studies. Thus, while some knowledge of the trends in the Reynolds stresses is available from physical measurements and from computation in direct numerical simulations (DNS), such data mostly serve to provide a target for empirical turbulence modelling but do not expose the underlying reasons for how and why the Reynolds stresses are manifested in the flow. In the same vein, DNS calculations have made possible the precise evaluation of budgets revealing the relative importance of the various physical effects contributing to the Reynolds stress distribution (Mansour, Kim & Moin 1988; Boudjemadi *et al.* 1997; Dimitropoulos *et al.* 2001; Wu & Moin 2009). While such information can help in developing empirical formulae suitable for a particular flow field, the passage from such knowledge to accurate yet general models of the terms in the transport equations remains elusive.

The earliest and most widespread suppositions about transport centre on the adoption of mean gradient diffusion laws by hypothesizing that transport due to the mixing of random eddies in the presence of a mean field should be analogous to the way in which randomly moving molecules produces diffusion in the presence of gradients in such quantities as momentum, heat and contaminant concentration (Bernard & Wallace 2002). The questionable nature of this analogy has long been noted (Corrsin 1974) and helps to explain the limited success of eddy viscosity models in representing turbulent flow. Moreover, careful testing of the eddy viscosity idea using accurate data from DNS and experiments in a variety of flows (Schmitt 2007) shows that it is of very restricted validity. It is also the case that the physics of transport cannot be accommodated by merely incorporating nonlinear or higher-order terms containing mean velocity derivatives, since counter-examples to the success of any such model exist. In fact, it appears to be inescapable that any physically valid turbulent transport theory must be constructed as a non-local model that lets the Reynolds shear stress at a point depend on flow properties in a surrounding spatial or temporal region.

Within the context of gradient transport modelling, non-local determinations of the eddy viscosity have been developed. These include a later result of Prandtl (1942) which was proposed as an alternative to his earlier mixing length theory (Prandtl 1925). In this, the eddy viscosity depends on computing a difference in mean velocities over the size of turbulent eddies. Yoshizawa (1984) used a two-scale direct interaction formalism to develop a generalization of the gradient model including a third derivative of the mean velocity. In effect, the approach has the character of a multi-point model. This formalism was found to be able to account for the breakdown of the eddy viscosity model in asymmetric turbulent shear flows.

Egolf (1994, 2009) and Egolf & Weiss (1998) proposed an advance beyond the Prandtl (1942) non-local eddy viscosity model, known as the difference-quotient turbulence model, in which the mean velocity difference replaces the mean velocity gradient. The resulting non-gradient model is non-local and attempts to account for eddies of all sizes in producing transport. The method has been applied successfully to wake and jet flows, among others. A fully non-local approach to modelling transport was developed by Hamba (2005, 2013) in which the Reynolds stress at any point

is expressed as a space–time integral of the mean velocity gradient weighted by an eddy viscosity determined from a velocity fluctuation response function. In channel flow, the Reynolds stress at a given location becomes a weighted integral of the mean velocity derivative across the channel. The response function and corresponding eddy viscosity distribution were evaluated using DNS data and revealed how the local Reynolds stress depends on a wide non-local region of the surrounding flow.

Important insights into the Reynolds stress have also come from recognition that there is a causal relationship between organized vortical structure in the boundary layer and Reynolds shear stress (Bernard, Thomas & Handler 1993). Elucidation of this relationship has been a principal objective of efforts at understanding the nature and dynamics of wall vortices. From such considerations, it has been shown that physically observed Reynolds stress distributions can be matched with random arrangements of Λ-shaped vortical structures in the boundary layer (Perry & Chong 1982). While insightful, and clearly based on non-local ideas, there has yet to be developed a systematic way of turning these insights into practical predictive schemes.

The origins of the Reynolds stress can also be considered from the point of view of the Lagrangian dynamics of fluid particle paths, as revealed in DNS, or possibly through paths measured in physical experiments (Toschi & Bodenschatz 2009). In particular, the Reynolds shear stress is an average of events in the flow field, each of which has a representation within the upstream history of the velocity field. One way to access such information is by considering the prior history of the velocity associated with fluid particles that arrive at given places at given times to create the correlation between velocity components that is contained in the Reynolds shear stress. Such a methodology of using backward fluid particle paths was previously developed and applied to a study of the Reynolds shear stress within $y^+ = 37$ of the wall in a low-Reynolds-number turbulent channel flow (Bernard & Handler 1990; Handler *et al.* 1992). This analysis was able to provide a detailed assessment of the validity of the assumptions surrounding the gradient transport model. Specifically, a mixing time was computed and the conflict between the mixing length and a local linear approximation to the mean velocity field was examined in detail. Also considered was the effect on transport of fluid particle accelerations during the mixing time.

Since the era in which the study described in Bernard & Handler (1990) was performed, DNS calculations of channel flow have increased dramatically in Reynolds number, domain size and transient extent. Data from such modern simulations afford an opportunity to revisit the analysis of Reynolds shear stress via backward particle paths from a more comprehensive perspective. Of great help in such an effort is the Johns Hopkins University online database (Li *et al.* 2008; Graham *et al.* 2016) of closely spaced realizations of the complete channel flow velocity field at $Re_\tau = U_\tau h/\nu = 999.35$, where h is the half-channel width, $U_\tau = \sqrt{\nu\, \mathrm{d}\overline{U}/\mathrm{d}y(0)}$ is the friction velocity, $\overline{U}(y)$ is the mean streamwise velocity, ν is the kinematic viscosity and y is the wall-normal coordinate. In comparison, the simulation in Bernard & Handler (1990) had $Re_\tau = 125$ and was limited to the region out to $y^+ = 37$. In the present work, the transport physics is studied for a complete channel including the wall to the centreline at $y^+ \equiv yU_\tau/\nu = 1000$.

Lagrangian particle path data are utilized here to analyse the cause of the Reynolds shear stress at different locations across the channel. This includes discerning the relative contributions of displacement and acceleration effects, considering some of the statistical properties of the backward particle paths, and computing the time scales associated with turbulent mixing. Attention is focused on exploring the causative factors leading to the Reynolds shear stress and pinpointing the essential physics

that needs to be captured if an accurate Reynolds stress model is to be developed. Some preliminary steps are taken towards developing a Reynolds stress model that incorporates the transport mechanisms revealed by this study.

2. Methodology

It is appropriate when exploring the origins of turbulent transport correlations to focus on channel flow, since the Reynolds shear stress, $\overline{uv}$, accounting for the transport of streamwise momentum in the wall-normal direction can be considered in isolation from other effects. In particular, the average Navier–Stokes equation in this case consists of

$$0 = -\frac{1}{\rho}\frac{\partial \overline{p}}{\partial x} + \frac{\partial}{\partial y}\left(v\frac{\partial \overline{U}}{\partial y} - \overline{uv}\right), \tag{2.1}$$

where x, y, z and U, V, W respectively represent coordinates and velocity components in the streamwise, wall-normal and spanwise directions respectively. The overbar denotes planar or time averaging, p is the pressure, ρ is the density and the fluctuating velocity components are u, v, w. The Reynolds shear stress is the sole unknown function preventing closure to the mean momentum equation. Traditional modelling of the Reynolds shear stress assumes that

$$\overline{uv} = -v_T \frac{\mathrm{d}\overline{U}}{\mathrm{d}y}, \tag{2.2}$$

where v_T is the eddy viscosity. The goal of the following is to further explore the physics behind $\overline{uv}$ so as to better understand the limitations of (2.2) and how improved formulae might be developed.

Understanding of $\overline{uv}$ can come from determining how the flow dynamics creates a correlation between u and v. In particular, let U_a, V_a be the velocities at a given point $\boldsymbol{x} = \boldsymbol{a}$ at time t. Then,

$$U_a = \overline{U}_a + u_a, \tag{2.3}$$
$$V_a = v_a \tag{2.4}$$

in channel flow and $\overline{u_a v_a}$ is the Reynolds shear stress at point $\boldsymbol{a}$. For each realization of the flow field, a fluid path, say $\boldsymbol{X}(\boldsymbol{a}, s)$, intersects $\boldsymbol{a}$ at time t so that $\boldsymbol{X}(\boldsymbol{a}, t) = \boldsymbol{a}$. At an earlier time, say $t - \tau$, the fluid particle that will later arrive at $\boldsymbol{a}$ at time t will be located at the point $\boldsymbol{b} = \boldsymbol{X}(\boldsymbol{a}, t - \tau)$. For channel flow, it follows that

$$U_b = \overline{U}_b + u_b, \tag{2.5}$$
$$V_b = v_b, \tag{2.6}$$

where $\overline{U}_b$ is random because $\boldsymbol{b}$ is random, while u_b and v_b are random both because of $\boldsymbol{b}$ but also because the fluctuating velocity field itself is random. For τ large enough, say $\tau > \tau_m$, the correlation $\overline{u_b v_a} = 0$. This means that within the time interval τ_m, events transpire within the flow to cause u_b, or equivalently U_b, to develop a correlation with v_a where it had no such correlation with v_a for $\tau > \tau_m$.

According to the identity

$$\overline{u_a v_a} = \overline{u_b v_a} + \overline{(\overline{U}_b - \overline{U}_a)v_a} + \overline{(U_a - U_b)v_a}, \tag{2.7}$$

for $\tau > \tau_m$, (2.7) reduces to

$$\overline{u_a v_a} = \overline{(\overline{U}_b - \overline{U}_a)v_a} + \overline{(U_a - U_b)v_a}, \tag{2.8}$$

which is a decomposition of the Reynolds shear stress into two fundamental contributions arising out of the dynamical behaviour of the flow field. The first represents a coupling between the wall-normal fluctuation v_a and the change in the local mean fluid velocity during the trajectory of fluid particles. In fact, this displacement transport effect, herein denoted for later convenience as

$$\Phi_D = \overline{(\overline{U_b} - \overline{U_a})v_a}, \tag{2.9}$$

is a precise way of expressing the traditional mixing idea promulgated in Prandtl's mixing length theory, although without the limitation to linear variation in the mean velocity difference. The second term on the right-hand side of (2.8), which will be henceforth denoted as

$$\Phi_A = \overline{(U_a - U_b)v_a}, \tag{2.10}$$

couples v_a with the acceleration of fluid particles during the mixing time. The attempt to sidestep such effects motivated Taylor (1932) to prefer a vorticity transport closure. Evaluation of (2.7) using DNS data in channel flow can provide insight into the origin of the Reynolds shear stress that may be used as the basis for future modelling decisions.

To acquire well-averaged estimates of the terms in (2.7) for a number of positions spanning a channel flow, it is required to collect large numbers of particle paths having common terminal points. In view of the spanwise homogeneity of channel flow, however, the commonality of the path end points only has to include the y^+ position. Consequently, many statistically independent particle paths can be obtained by marching particles from fixed y^+ planes backward in time.

3. Computational technique

The channel flow data used in this study were obtained from a DNS whose computed velocity field is provided as part of the Johns Hopkins turbulence database (Li *et al.* 2008). The simulation incorporates periodic boundary conditions in the longitudinal and transverse directions and a no-slip boundary condition on the top and bottom walls. The wall-normal velocity–vorticity formulation of the Navier–Stokes equation is solved using a Fourier–Galerkin pseudo-spectral method in the longitudinal and transverse directions and a seventh-order basis-splines collocation method in the wall-normal direction. Initially, the flow is driven by a constant volume flux control. Once stationary conditions are reached, the control is changed to a mean pressure gradient forcing term. More specific simulation details including validation of the solutions have been given by Perlman *et al.* (2007), Li *et al.* (2008) and Graham *et al.* (2016).

The particular simulation used here has Reynolds number $Re_\tau = 999.35$ based on the friction velocity and channel half width. In terms of the centreline velocity, the Reynolds number is $Re_c = 22\,625$. The grid in the simulation has $2048 \times 512 \times 1536$ mesh points in the x, y and z directions respectively. The scaled viscosity $\nu = 5 \times 10^{-5}$ and the scaled mean pressure gradient driving the flow is $\mathrm{d}\overline{p}/\mathrm{d}x = 0.0025$. Velocity data from the simulation are stored over the interval $0 \leqslant t \leqslant 25.9935$ in time increments of $\Delta t = 0.0013$ (Graham *et al.* 2016). In terms of wall units, the time interval is $0 \leqslant t^+ \leqslant 1298$ and $\Delta t^+ = 0.0649$.

The collections of paths are identified according to the y^+ planes of their end points, in which case they are computed by an integration backward in time. The particular y^+ values used in the data sets are listed in table 1. At the given ending times, 4704

y^+	ΔT	τ	N	N_p
1.9	0.25	16.12	72	338 688
2.8	0.25	12.48	80	376 320
3.8	0.25	11.44	88	404 712
6.4	0.50	8.32	40	188 160
8.9	0.50	9.36	40	188 160
11.4	1.00	10.92	28	131 712
14.0	0.50	8.32	40	188 160
31.2	0.50	5.98	64	301 056
54.8	0.50	5.46	72	338 688
84.8	0.50	5.20	72	338 688
121.0	1.00	5.46	40	188 160
163.0	1.00	6.24	20	94 080
211.0	1.00	6.76	26	122 304
264.0	1.00	7.80	26	122 304
322.0	1.00	8.58	34	159 936
385.0	1.00	8.84	32	150 528
452.0	1.00	10.92	26	122 304
523.0	0.50	13.00	52	244 608
597.0	1.00	11.70	26	122 304
673.0	1.00	11.96	20	94 080
752.0	1.00	12.74	20	94 080
832.0	0.50	13.78	22	103 488
914.0	0.50	16.12	30	141 120

TABLE 1. Table of data collected at various y^+ positions. Here, ΔT is the approximate time difference between the ending times of particle data sets, τ is how long each data set was run back in time, N is the total number of data sets collected at each y^+ location and N_p is the total number of paths at the specified y^+ location.

positions of the paths are uniformly spread out over each of the y^+ planes within the simulation domain. The symmetry of the channel flow is taken advantage of by launching half of the fluid particles from the top half of the channel and the other half from a symmetrically placed plane on the bottom half.

In order to obtain smooth statistics, multiple ending times are used for many of the y^+ positions, as is denoted by N in table 1. Here, ΔT indicates the time interval between the ending times of the particles at each y^+ location. The data sets at each ending position were marched back in time over an interval τ, as is also indicated in table 1. For each y^+ position, τ was set to be large enough so that $\overline{v_a u_b}$ had reached zero.

Paths were computed using a fourth-order Runge–Kutta method with time step $\Delta t = 0.0013$. Spatial interpolation was carried out via a fourth-order Lagrangian scheme and the temporal interpolation used a piecewise cubic Hermite interpolating polynomial (PCHIP). The spatial and temporal interpolations are applied automatically when the database is accessed.

The accuracy of the paths was determined by computing the motion of $N_p = 1536$ particles from evenly spaced grid positions at time $t = 0.52$ backward over the time interval [0.52, 0] at three different y^+ locations. The particle path simulation was conducted for $\Delta t_k = 0.0013/2^k$, $k = 0, 1, 2, \ldots, 6$, where Δt_k is the time step resolution for the Runge–Kutta method. Denoting the backward path of the ith particle
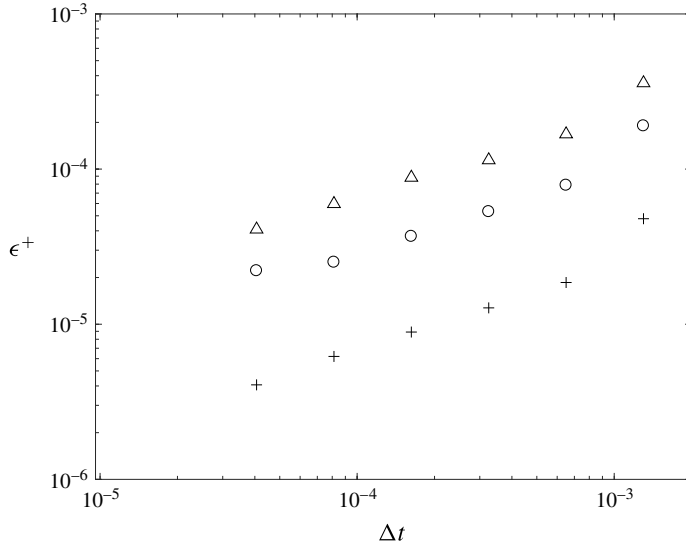
FIGURE 1. Root-mean-square positional errors for particle paths at different y^+ levels: $\bigcirc$, $y^+ = 3.8$; $\triangle$, $y^+ = 14$; $+$, $y^+ = 322$.

at a specific Δt_k as $X_k^i(\boldsymbol{a}, t)$, then the root-mean-square difference between the finest resolution path that has Δt_6 and paths for which $k < 6$ is defined by

$$\epsilon_k^+(t) = \left\{ \frac{1}{N_p} \sum_{i=1}^{N_p} |X_k^i(\boldsymbol{a}, 0) - X_6^i(\boldsymbol{a}, 0)|^2 \right\}^{1/2}. \tag{3.1}$$

Figure 1 contains a plot of $\epsilon_k^+(t)$ calculated for Δt_k, $k = 0, 1, 2, \ldots, 5$, showing that at all three y^+ levels, the errors are converging to zero with smaller Δt. In an additional test, the entire data set for points ending at $y^+ = 14$ was replicated with $\Delta t = 0.0013/4$, and only inconsequential differences in the various statistical quantities containing velocities were found. This suggests that data computed with a smaller Δt than is used here would not yield a different analysis of the transport decomposition and other statistics.

It proves convenient in what follows to base all discussions of the Reynolds stress on the trends in the lower half of the channel where $\overline{uv} < 0$. To accomplish this, the data taken in the top half of the channel are mapped to the lower half by changing the sign of the v velocity component and taking the mirror image of paths through the midplane of the channel.

4. Mixing time

The decomposition of the Reynolds shear stress given in (2.8) is valid once τ is large enough so that $\overline{u_b v_a} = 0$. The minimum time at which this happens, say τ_m, is one over which fluctuations in u and v develop correlation, and is a natural candidate to be the mixing time. Figure 2 shows the computed behaviour of $\overline{u_b v_a}$ as a function of τ^+ for fluid particles whose paths end on planes between 54.8 and 914, while figure 3 shows similar results for paths terminating on y^+ planes between 1.9 and 54.8.
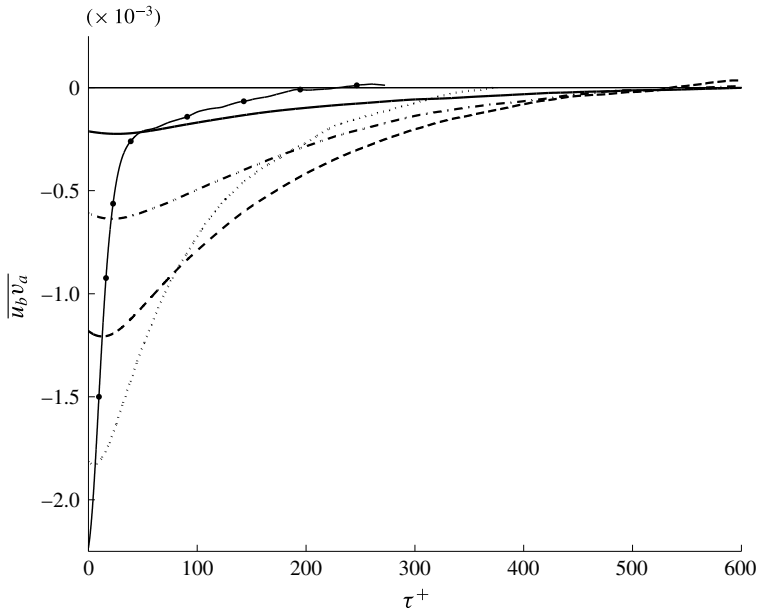
FIGURE 2. The behaviour of $\overline{u_b v_a}$ computed for paths ending at different y^+ values: —●—, $y^+ = 54.8$; ······, $y^+ = 264$; – – –, $y^+ = 523$; — · —, $y^+ = 752$; ——, $y^+ = 914$.
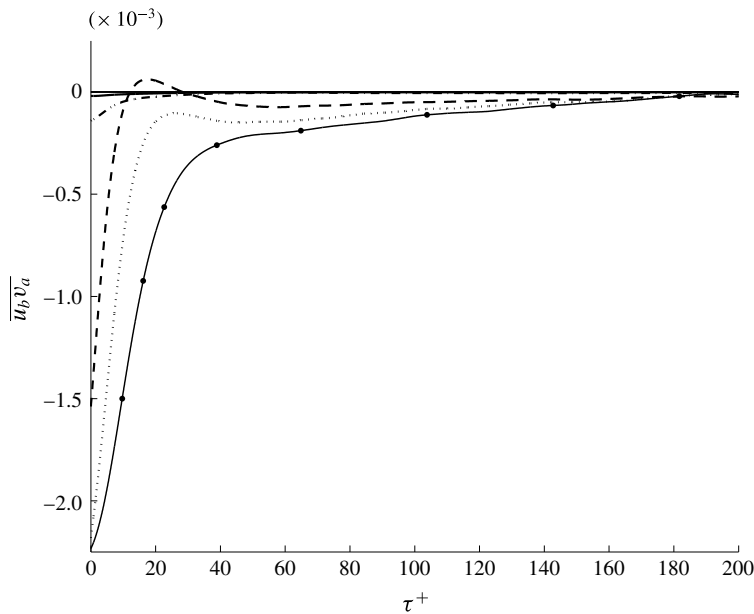

FIGURE 3. The behaviour of $\overline{u_b v_a}$ computed for paths ending at different $y^+ =$ values: —●—, $y^+ = 54.8$; ······, $y^+ = 31.2$; – – –, $y^+ = 14$; — · —, $y^+ = 3.8$; ——, $y^+ = 1.9$.

Considering the outer region given in figure 2, it is seen that in each case the $\overline{u_b v_a}$ correlation is largest in magnitude at $\tau^+ = 0$ and decreases monotonically in magnitude with τ^+. The value of τ_m^+ increases for y^+ locations up to 500 and then

is approximately constant beyond this point. For these data, the determination of τ_m^+ is readily found from the locations where $\overline{u_b v_a}$ first goes to zero. Consideration of the $\overline{u_b v_a}$ correlation curves closer to the wall in figure 3 reveals that the situation is somewhat more complex in this case. In particular, as y^+ moves towards the wall from $y^+ = 54.8$, the $\overline{u_b v_a}$ curves drop off in magnitude towards zero increasingly rapidly with τ^+, but at the same time they acquire long-lived tails of small correlation before eventually going to zero. Moreover, there is a tendency for some of the $\overline{u_b v_a}$ curves to reverse their monotonic fall in magnitude before finally regaining their relaxation towards zero. For the data in the approximate range $8 \leqslant y^+ \leqslant 20$ and illustrated by the $y^+ = 14$ curve in figure 3, $\overline{u_b v_a}$ changes sign before changing sign a second time and then slowly relaxing back towards zero. For such curves, the zero crossings at small times do not represent the end of correlation and so cannot be taken as the value of τ_m^+ that is called for under its current definition. Moreover, for the curves in figure 3, the presence of a long non-zero tail means that the eventual time at which correlation technically does end is not necessarily more physically meaningful than lesser values of τ^+ where the correlation is small but not exactly zero. This suggests that a decomposition of $\overline{u_a v_a}$ based strictly on τ_m^+ may not be the most advantageous choice for all points in the channel.

The region near the wall where the anomalous behaviour of the mixing time occurs is one where it is well known that vortical structures of substantial streamwise extent are present. These are vortices whose signatures in the velocity field are low-speed streaks as well as rapid burst and sweep motions associated with the Reynolds shear stress (Bernard *et al.* 1993; Bernard 2013). It is plausible that the trends in figure 3 reflect the presence of relatively long-lived structures that promote correlation over long time periods. We will return to this point subsequently.

Some insight into how best to define a time for the purposes of decomposing $\overline{u_b v_a}$ can be had by considering the trends in the decomposition in (2.7) as a function of the time delay τ^+. For this purpose, figures 4–6 show this result for points $y^+ = 8.9$, 84.8 and 673 respectively, encompassing different regions of the flow. In each of these, the behaviour of $\overline{u_b v_a}$ may be seen to be consistent with what was discussed in terms of figures 2 and 3. It can be noticed that the sum of the curves in each of figures 4–6 returns $\overline{u_a v_a}$, as expected.

The displacement transport term Φ_D in each case decreases in value towards a minimum that is in the neighbourhood of $\overline{u_a v_a}$ before rising back towards zero. In fact, the long-time trend in Φ_D, as seen clearly in figures 4 and 5, is to follow a slow relaxation towards zero beyond the minimum. The limiting value of Φ_D is expected to be zero since ultimately

$$(\Phi_D)_{\tau^+ \to \infty} = \overline{v_a \overline{U}_{b_\infty}} = 0 \tag{4.1}$$

in channel flow where correlation between v_a and $\overline{U}_b$ should presumably be non-existent for very large τ^+.

In contrast to the trends in Φ_D, for the three times in figures 4–6, the acceleration affect Φ_A moves towards a positive maximum at relatively short times. For larger τ^+, Φ_A diminishes and for the data at $y^+ = 8.9$ and 84.8 becomes negative within the view shown in the figures. For the data at $y^+ = 673$, Φ_A is still positive as far as the data were computed but is steadily decreasing beyond this point. In fact, in all cases, given enough time, Φ_A will diminish towards $\overline{u_a v_a}$, with the latter limit resulting from the fact that

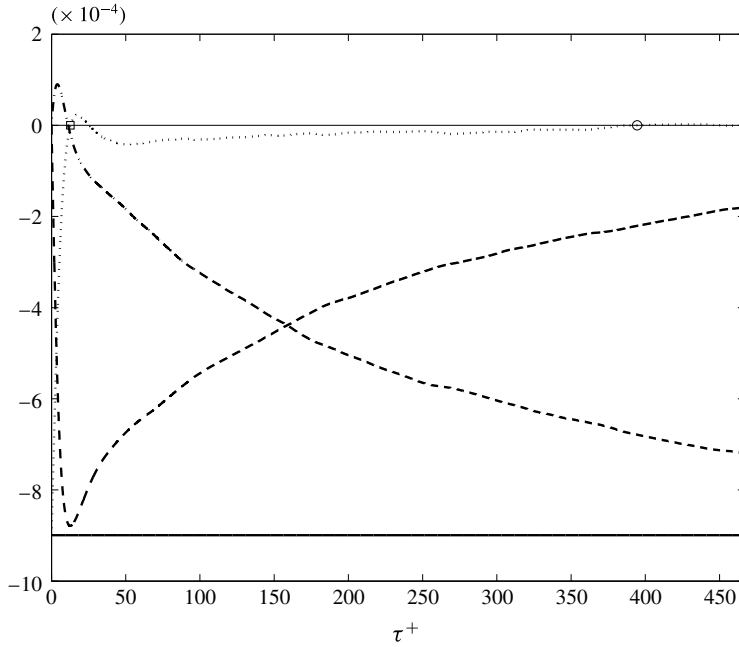$$(\Phi_A)_{\tau^+ \to \infty} = \overline{v_a U_a} - \overline{v_a \overline{U}_{b_\infty}} = \overline{u_a v_a}. \tag{4.2}$$

FIGURE 4. Decomposition in (2.7) at $y^+ = 8.9$: $\cdots\cdots$, $\overline{u_b v_a}$; $---$, Φ_D; $-\cdot-$, Φ_A; ——, $\overline{u_a v_a}$. The square on the τ^+ axis denotes τ_D^+ and the circle denotes τ_m^+.
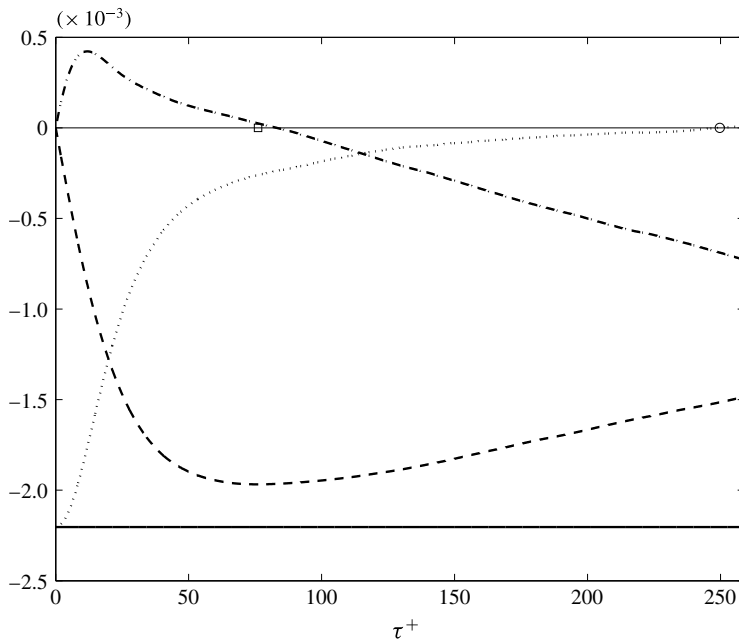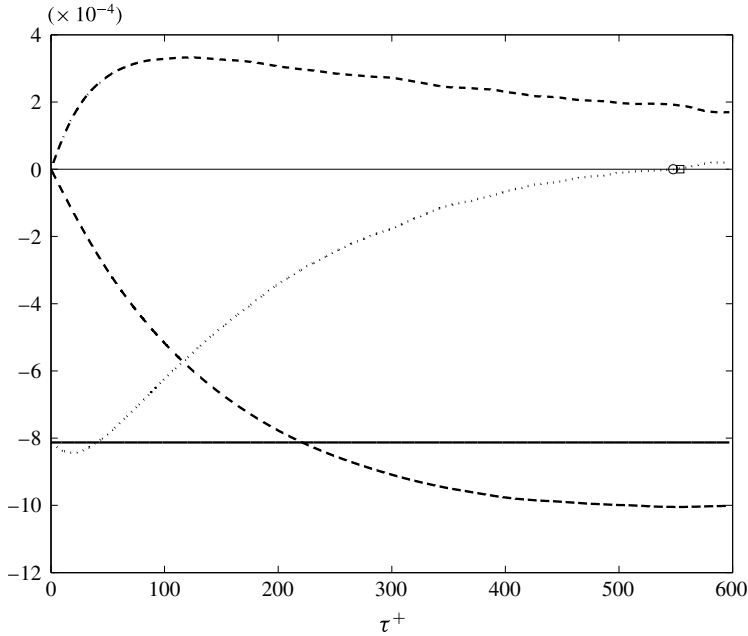

FIGURE 5. Decomposition in (2.7) at $y^+ = 84.8$: $\cdots\cdots$, $\overline{u_b v_a}$; $---$, Φ_D; $-\cdot-$, Φ_A; ——, $\overline{u_a v_a}$. The square on the τ^+ axis denotes τ_D^+ and the circle denotes τ_m^+.

FIGURE 6. Decomposition in (2.7) at $y^+ = 673$: $\cdots\cdots$, $\overline{u_b v_a}$; $---$, Φ_D; $-\cdot-$, Φ_A; ——, $\overline{u_a v_a}$. The square on the τ^+ axis denotes τ_D^+ and the circle denotes τ_m^+.

Thus, the asymptotic behaviour of both Φ_D and Φ_A depends on equal and opposite relaxation of $\overline{v_a \overline{U}_b}$ to zero. This accounts for the trends in Φ_D and Φ_A as seen for large τ^+ values.

The displacement transport term in and of itself reflects the classical idea of the mixing process by which eddies exchange momentum with the surrounding fluid within the presence of a variable mean velocity field. Viewed in this way, the time delay, say τ_D^+, where the displacement term is at a minimum and thus makes its greatest contribution to a negative $\overline{u_a v_a}$ is also a natural candidate to choose for the mixing time. In fact, τ_D^+ has intrinsic physical meaning as reflecting the time at which the strongest internal connection occurs between the seemingly random values of v_a and upstream events that carry momentum of fluid particles through the flow, leading to a net transport of momentum at a given point. The dominance of displacement physics is also evident in the fact that at τ_D^+ for each y^+, Φ_D makes the only large contribution to $\overline{uv}$. Moreover, it will also be seen below that flow events contributing to Φ_D occur much more frequently than those contributing to the other terms on the right-hand side of (2.7).

In each of the figures 4–6, τ_m^+ and τ_D^+ are indicated. For figure 6, it is seen that these times are identical, while for $y^+ = 84.8$ and then $y^+ = 8.9$ they are increasingly far from each other. In the case of figure 4, the two scales diverge consistent with the previous observation that at points near the wall $\overline{u_b v_a}$ develops a long tail of small correlation that carries the precise value of τ_m^+ to points distant from the range of times where most of the reduction in the correlation has occurred. This suggests that the scale τ_D^+ is more relevant to the main body of physics surrounding the shear stress correlation near the wall than is the last zero crossing in $\overline{u_b v_a}$.

The complete trends in τ_m^+ and τ_D^+ across the channel are shown in figure 7(a), while figure 7(b) is a detailed view of τ_D^+ near the wall. It is seen in figure 7(a)
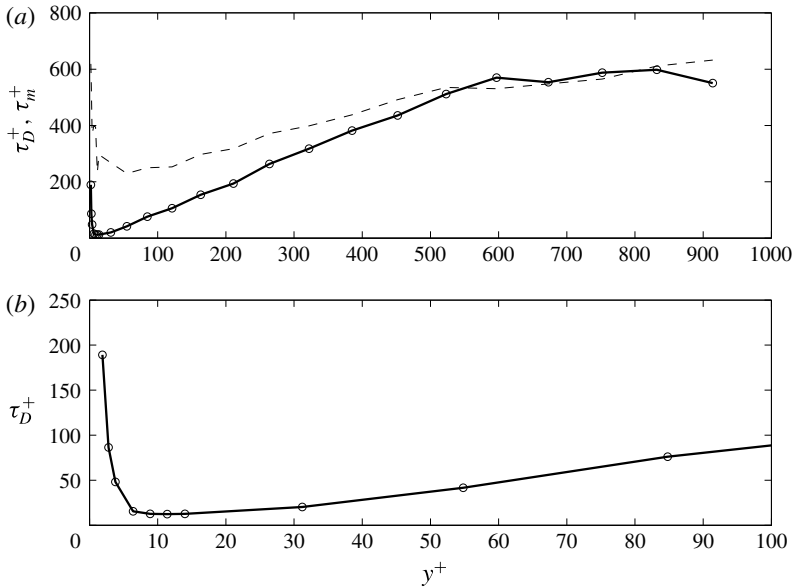
FIGURE 7. Time scales in channel flow: ——, τ_D^+; – – –, τ_m^+. (*a*) Entire channel; (*b*) close up of the near-wall region.

that beyond $y^+ = 500$, $\tau_m^+ \approx \tau_D^+$, while closer to the wall, τ_m^+ remains relatively large and is somewhat erratic. In the viscous sublayer, τ_m^+ is very large and reflects the presence of the long tails of slight correlation in $\overline{u_b v_a}$ seen in figure 3. A similar rise in τ_m^+ near the boundary was observed in the previous study (Bernard & Handler 1990) at lower Reynolds number. In that case, the available time to simulate paths was insufficient to accommodate the complete time interval τ_m^+ near the wall. This is not a limitation in the current work, where the simulated field covers more than sufficient time to evaluate τ_m^+ at all points. Finally, it may be noticed that τ_D^+ attains a minimum at $y^+ \approx 10$ that is an order of magnitude smaller than it is at its near-wall and far-wall peaks. This is testimony to the intensity of turbulent mixing close to the wall where the Reynolds stresses are highest. Evidently, the mechanics of transport physics is considerably different in this region than it is in the outer channel where Φ_D evolves over a relatively long time.

In view of the special significance of τ_D^+, our analysis of the physical causes of the Reynolds shear stress will be based on evaluating the decomposition in (2.7) at this time at all points across the channel. Viewed from this perspective, $\overline{u_a v_a}$ is decomposed into the sum of the natural displacement transport term plus corrections reflecting acceleration effects and whatever residual correlation may be occurring in $\overline{u_b v_a}$, with the latter appearing to be associated with long-time effects of vortical structures in the near-wall region.

Figure 8 shows the Reynolds stress decomposition across the channel computed from the fluid paths used in this study. This is obtained by evaluating each of the terms in (2.7) at the computed value of τ_D^+ at the local y^+ position. The dominance of the displacement effect is seen to span the channel, showing that the classical physics of transport in a variable mean velocity field accounts for by far the largest share of the total transport. The effect of the long tails in $\overline{u_b v_a}$ is felt as a small negative contribution to the Reynolds shear stress near the wall. This effect is negligible for $y^+ \geqslant 400$. The acceleration transport is negative close to the wall and then beyond
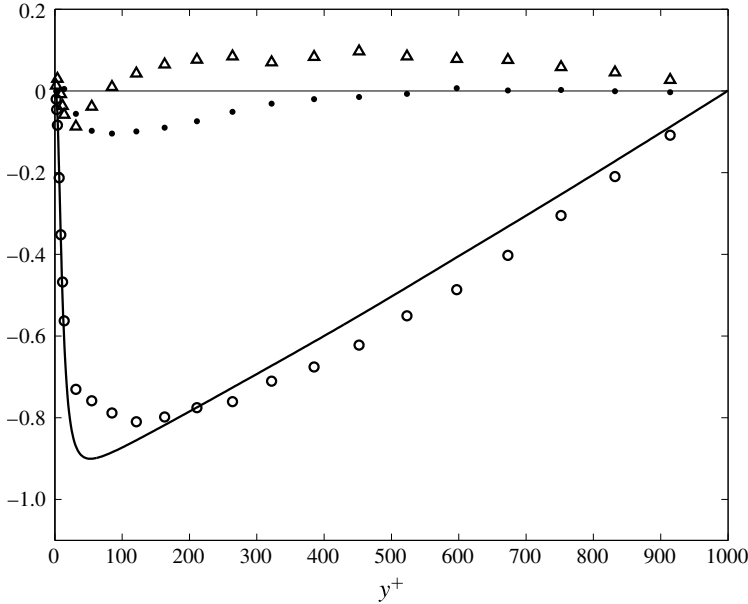
FIGURE 8. Evaluation of (2.7) at τ_D computed across the channel: ——, $\overline{u_a v_a}$; ◯, Φ_D; △, Φ_A; ●, $\overline{u_b v_a}$.

$y^+ = 100$ is a small, approximately constant, positive value over a large region that diminishes to zero at the channel centreline.

A detailed view of the decomposition in (2.7) near the wall is shown in figure 9(*a*). This establishes that the displacement term can account entirely for the Reynolds shear stress in the viscous sublayer out to approximately $y^+ = 15$. Beyond this point, until $y^+ \approx 100$, the acceleration term is negative at these distances from the wall. Figure 9(*b*) reproduces the similar partition of the Reynolds shear stress as computed in the previous backward particle path study at a much lower Reynolds number (Bernard & Handler 1990). The qualitative agreement in the role of the displacement term near the wall and the negativity of the acceleration effect is apparent.

In the earlier simulation by Handler *et al.* (1992), the acceleration term was further decomposed into the effects of pressure and viscous forces by integrating the Navier–Stokes equation along a particle path to yield an expression for $U_a - U_b$. The result is

$$\Phi_A = -\frac{1}{\rho} \int_b^a \overline{v_a \left(\frac{\partial P}{\partial x} \right)_b} \, ds + \nu \int_b^a \overline{v_a (\nabla^2 U)_b} \, ds, \tag{4.3}$$

showing how acceleration transport depends on the effect of viscous and pressure forces. The previous evaluation of (4.3) showed that the viscous effect dominated until $y^+ = 40$, giving way to pressure effects beyond this point. It is reasonable to then expect that the acceleration effect seen in figure 8 for $y^+ > 40$ is a result of the pressure term only. Consequently, the change in sign in the acceleration term at $y^+ = 100$ should reflect a change in how the pressure contributes to transport. Near the wall, the negative contribution from acceleration transport may be associated with a relatively small number of flow events in which ejecting fluid particles ($v_a > 0$) are decelerated and sweeping particles ($v_a < 0$) are accelerated. Such events can be traced to the way in which fluid particles are affected by the presence of tilted
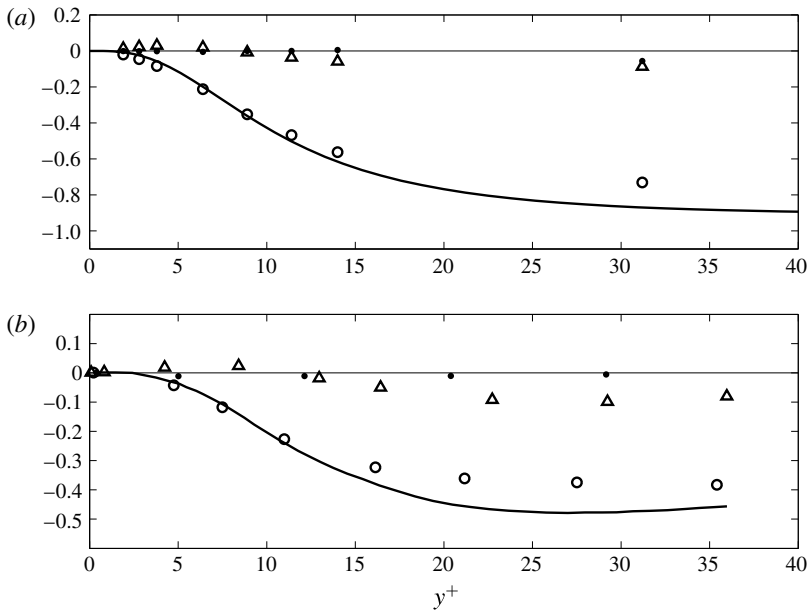
FIGURE 9. Evaluation of (2.7) at τ_D in the near-wall region: (*a*) data at $R_\tau = 1000$ (Graham *et al.* 2016); (*b*) data at $R_\tau = 125$ (Bernard & Handler 1990); ——, $\overline{u_a v_a}$; $\circ$, Φ_D; $\triangle$, Φ_A; $\bullet$, $\overline{u_b v_a}$.

rotational regions, as would occur from quasi-streamwise vorticity (Handler *et al.* 1992; Bernard *et al.* 1993). Further from the wall where Φ_A is strictly positive, it appears that particles travelling towards the wall tend to decelerate and those moving away accelerate via the effect of pressure. This is a relatively constant effect that fits in with the natural idea of flow that decelerates travelling towards the boundary and accelerates as it moves away from the boundary.

Another way of viewing the present results is shown in figure 10, in which the Reynolds shear stress decomposition is between the displacement term and the sum of the remaining terms. This highlights the fact that over and above any modelling issues faced in capturing the displacement transport effect, an additional negative contribution to $\overline{uv}$ reflecting the physics of acceleration and the $\overline{u_b v_a}$ correlation is necessary to fully capture the peak amplitude of $\overline{uv}$ and to compensate for the small extent by which Φ_D overpredicts the Reynolds shear stress further from the wall.

5. Gradient transport

The gradient transport model of the Reynolds shear stress depends on the requirement that $\overline{U}(y)$ have a linear spatial variation over the region that fluid particles move to during the mixing time. In light of the previous discussion, the latter is taken here to be τ_D^+. In this case, we define

$$L = a - b, \qquad (5.1)$$

where

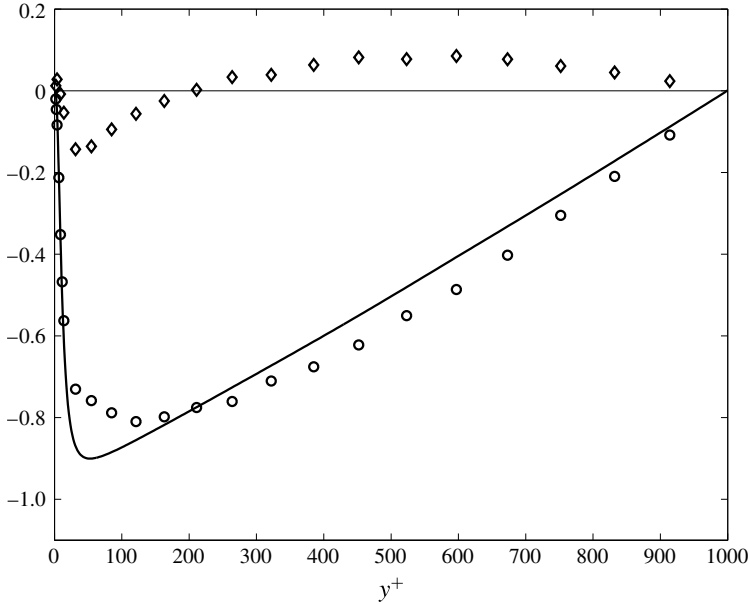$$L = \int_{t-\tau}^{t} U(X(s), s) \, ds \qquad (5.2)$$

FIGURE 10. Evaluation of (2.7) at τ_D computed across the channel: ——, $\overline{u_a v_a}$; $\bigcirc$, Φ_D; $\diamondsuit$, $\Phi_A + \overline{u_b v_a}$.

is the vector distance moved by fluid particles between $X(t - \tau) = \boldsymbol{b}$ and $X(t) = \boldsymbol{a}$. If it were the case that L_2 were small enough so that linearity of $\overline{U}$ could be claimed over this distance, then the Taylor series expansion of $\overline{U}_b$ about the point $\boldsymbol{a}$ could be truncated to the form

$$\overline{U}_b \approx \overline{U}_a - L_2 \frac{\mathrm{d}\overline{U}}{\mathrm{d}y}, \tag{5.3}$$

with higher-order terms omitted. Substitution of (5.3) into (2.9) gives

$$\Phi_D = -\overline{v_a L_2} \frac{\mathrm{d}\overline{U}}{\mathrm{d}y}. \tag{5.4}$$

Consequently, if a gradient transport law were valid, it would arise in the displacement transport term and would have an eddy viscosity given by

$$\nu_T = \overline{v_a L_2}. \tag{5.5}$$

By defining a Lagrangian autocorrelation function

$$f_{vv}(s) = \frac{\overline{v(X(t), t) v(X(t + s), t + s)}}{\overline{v(X(t), t)^2}}, \tag{5.6}$$

and substituting for L_2 using (5.2), (5.5) may be written as

$$\nu_T = \overline{v^2} T_{22}, \tag{5.7}$$

where T_{22} is a Lagrangian integral scale defined by

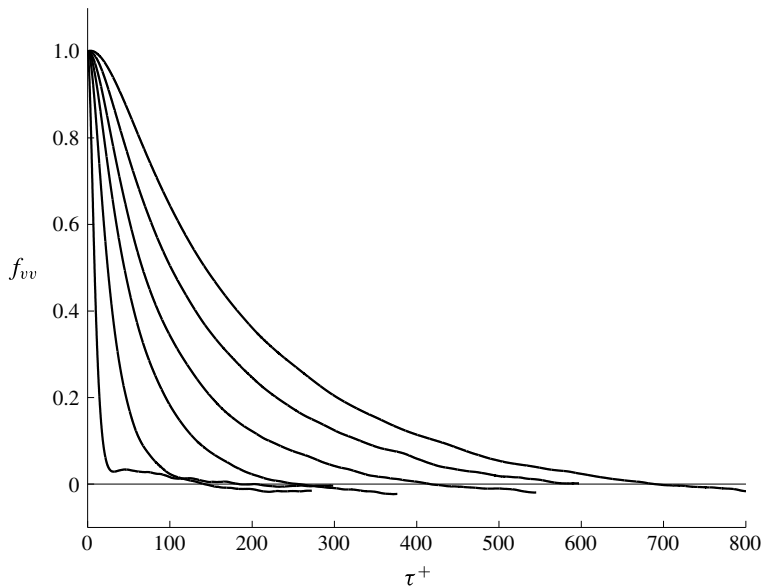$$T_{22} = \int_{-\infty}^{0} f_{vv}(s) \, \mathrm{d}s. \tag{5.8}$$

FIGURE 11. The computed correlation coefficient f_{vv} for paths arriving at $y^+ = 31.2$, 121, 264, 452, 673, 914 (curves increase in magnitude and extent with y^+, so the top curve is at $y^+ = 914$).

An indirect means of assessing the validity of a gradient model for the Reynolds shear stress in channel flow is to compare the rigorously derived eddy viscosity in (5.7) with the eddy viscosity that would be required to force the model in (2.2) to be accurate.

Using our ensembles of computed particle paths, the correlation functions f_{vv} can be evaluated and from this an estimate of T_{22}^+ can be determined. Figure 11 shows the computed trends in f_{vv} for $y^+ \geqslant 31.2$, while figure 12 has plots of f_{vv} in the near-wall region $y^+ \leqslant 14$. Considering figure 11, it is seen that the correlation measured by f_{vv} persists for longer times the further the ending plane of the paths is from the wall. The functions themselves display a smooth regularity apart from the curve closest to the boundary which has a slight maximum before decreasing to zero.

Near the wall, figure 12 shows a very much different story. Here, despite the use of large data sets, the f_{vv} correlation is quite noisy, becomes noisier as the wall is approached and includes an increasingly large second maximum similar to that in the curve at $y^+ = 31.2$ in figure 11. The phenomenon at work in the near-wall region consists of a large and rapid drop off in correlation in a short time followed by a long period of noisy correlation. Evidently, this behaviour must reflect the idiosyncrasies of flow in the thin viscous region, where long-time correlations are produced in the velocity field by the passage of vortical structure overhead. Apparently, until enough individual events are sampled, the statistics will not be as smooth as they are at points further from the wall.

The area under the f_{vv} curves is T_{22}^+, which can be evaluated by numerical quadrature. The result is shown in figure 13(*a*) for the whole channel and in figure 13(*b*) as a close up of the near-wall region. Evidently, T_{22}^+ varies linearly throughout most of the channel, including the region from approximately $y^+ = 25$ to $y^+ = 900$ where it begins to level off, since it must be relatively constant at the centreline due to symmetry. Close to the wall, T_{22}^+ is as large as it is at the centreline,
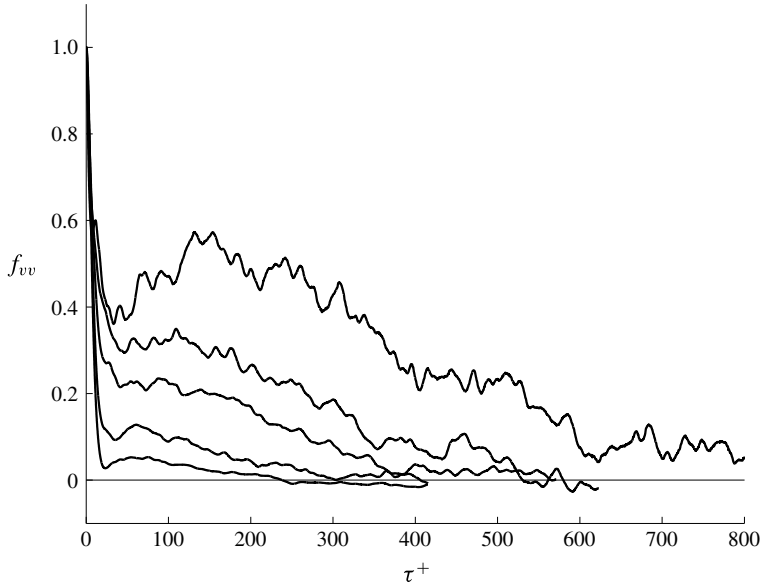
FIGURE 12. The computed correlation coefficient f_{vv} for paths arriving at $y^+ = 1.9$, 2.8, 3.8, 6.4, 14 (curves decrease in magnitude and extent as y^+ increases, so the top curve is at $y^+ = 1.9$).
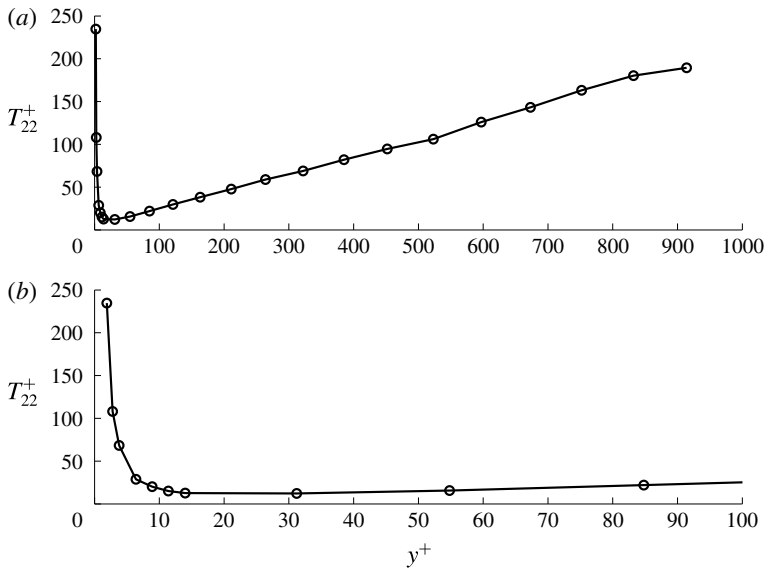

FIGURE 13. The behaviour of T_{22}^+ computed in channel flow: (*a*) across the channel; (*b*) close up of the near-wall region.

and it drops rapidly to its minimum near $y^+ = 15$. The behaviour of T_{22}^+ is not unlike that of τ_D^+ shown in figure 7, although it is approximately 1/3 as large in the central part of the channel.
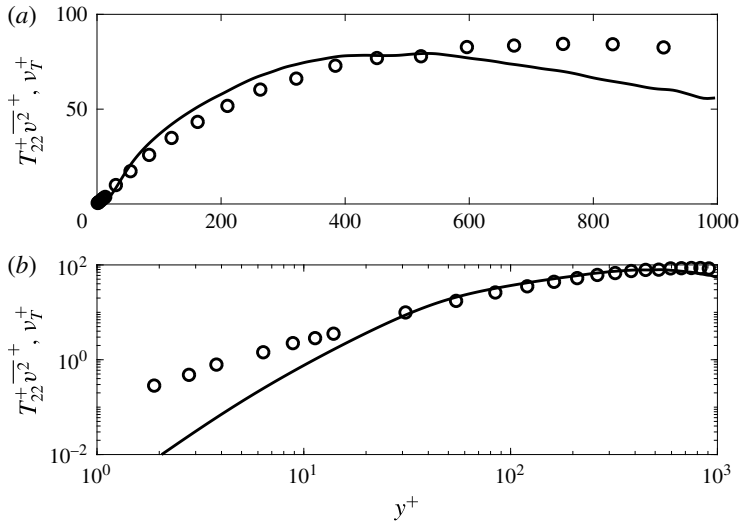
FIGURE 14. The eddy viscosity in channel flow: (*a*) comparison between $\bigcirc$, $T_{22}^+ \overline{v^2}^+$ and ——, ν_T^+; (*b*) log–log plot highlighting the near-wall behaviour.

Our main interest in T_{22}^+ is in combination with $\overline{v^2}^+$ to form the physically correct eddy viscosity. This is shown plotted in figure 14 together with the distribution of eddy viscosity that is guaranteed to lead to an accurate calculation of $\overline{U}$ via a gradient Reynolds stress model, namely

$$\nu_T = \frac{-\overline{uv}}{\mathrm{d}\overline{U}/\mathrm{d}y}. \tag{5.9}$$

Any disagreement between these eddy viscosities reflects how ν_T in (5.9) is essentially covering up errors deriving from non-gradient physics included within the displacement and acceleration transport terms as well as slight non-zero values of $\overline{u_b v_a}$. Figure 14(*a*), comparing (5.7) and (5.9), suggests that the most serious conflict in eddy viscosity occurs in the central region beyond $y^+ = 500$, where the physical eddy viscosity is approximately constant and the modelled version decreases. In the immediate neighbourhood of $y^+ = 500$, the exact and modelled eddy viscosities appear to be the same. Nearer the wall, the disagreement in eddy viscosities does not appear to be especially significant, although the closer look afforded by the log–log plot in figure 14(*b*) reveals some apparently small differences between the exact and modelled eddy viscosities that are both quantitative and qualitative.

To assess the impact that the differences in eddy viscosity have on how well gradient wall physics accounts for $\overline{uv}$, figure 15 compares (5.4) with the Reynolds shear stress. This shows that the small differences in figure 14(*b*) actually mean that the physics of gradient transport is entirely unsuitable as a model of the near-wall Reynolds stress. In contrast, somewhat ironically, for $y^+ \geqslant 400$, the gradient model is generally a good fit where the greatest differences in eddy viscosity are observed in figure 14(*a*). The latter observation must reflect the fact that the mean velocity in the central region of the channel in not far removed from a linear variation, and the mixing lengths for points beyond $y^+ = 400$ are such that fluid particles largely remain within the linear mean velocity field during the mixing time.
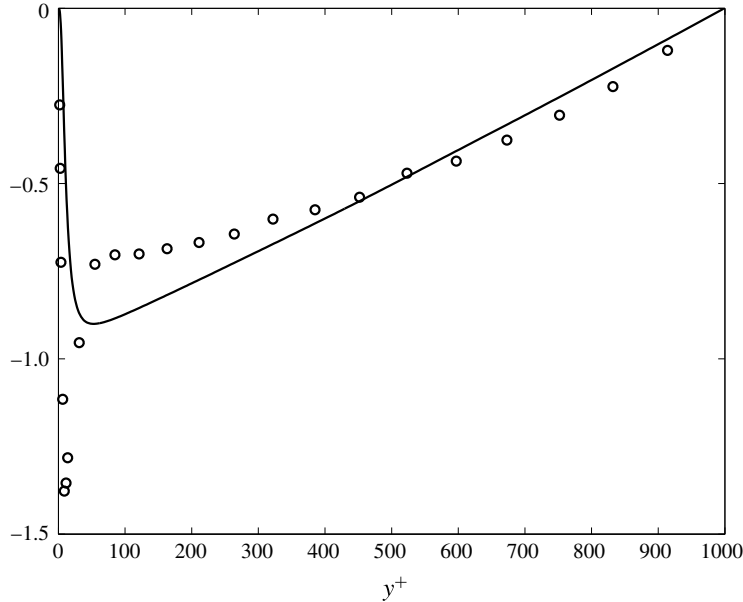
FIGURE 15. The inadequacy of gradient transport physics: ——, $\overline{uv}^+$;
$\bigcirc$, $-T_{22}^+\overline{v^2}^+ \, \mathrm{d}\overline{U}^+/\mathrm{d}y^+$.

In the idealized case of homogeneous shear flow, where $\overline{U}(y) = Sy$ and $S = \mathrm{d}\overline{U}/\mathrm{d}y$ is a constant shearing everywhere, it may be inferred from (5.4) and (5.7) that

$$\Phi_D = -\overline{v^2}T_{22}\frac{\mathrm{d}\overline{U}}{\mathrm{d}y} \qquad (5.10)$$

is an exact asymptotic expression for Φ_D for large τ. Thus, unlike channel flow, where (4.1) holds for large times, the infinite extent of the linear mean field in homogeneous shear flow has the consequence of eliminating the factors that would ordinarily work to decorrelate the displacement correlation after it forms. Moreover, the constancy of the asymptotic value of Φ_D means that the same is true of the acceleration term Φ_A. Thus, in this instance also, Φ_A persists as a potentially non-zero constant at large τ, despite the randomization of fluid particle trajectories.

6. Significant events leading to transport

Unlike the normal Reynolds stresses, where all samples of the velocity fluctuation make contributions to the mean value, the Reynolds shear stress is composed of many offsetting plus and minus contributions. Consequently, the value of $\overline{uv}$ at any point in the flow depends on the imbalance between plus and minus realizations. The net value of the correlation can therefore be viewed as the end result of the action of a subset of the total collection of realizations. Based on this idea, it becomes possible to get a somewhat more precise view of the factors that produce Reynolds shear stress as well as each of the terms on the right-hand side of (2.7) evaluated at time τ_D.

To implement this analysis in the case of $\overline{u_a v_a}$, we consider its value at a point in the lower half of the channel where it is negative. At such locations, events for
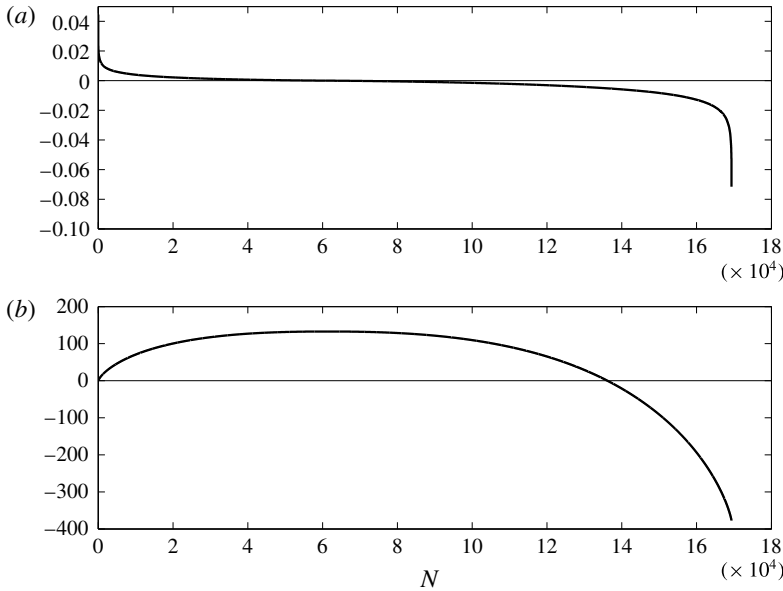
FIGURE 16. Contributions to $\overline{u_a v_a}$ at $y^+ = 54.8$ from a data set consisting of 169 344 points in lower channel half: (*a*) individual contributions ranked from largest to smallest; (*b*) cumulative sum of contributions in (*a*), showing zero crossing at $N_0 = 136\,176$.

which u_a and v_a have opposite sign take precedence over events where they have the same sign. The average $\overline{u_a v_a}$ is negative either because a decisive majority of events have oppositely signed pairs, or because a few very strong events tilt the average to be negative. A combination of both tendencies might also prevail. The ensembles of paths that have been computed afford an opportunity to investigate this question. Thus, for any y^+ value, we order the N paths that contribute to each of the correlations in (2.7) from the smallest to the largest contributors depending on the sign of the correlation. For example, for $\overline{u_a v_a}$ in the lower channel half, the ranking is from the most positive to the most negative, as shown in figure 16(*a*) for the data at $y^+ = 54.8$. Now, calculating partial sums $\sum_{i=1}^{n} u_a^i v_a^i$, $n = 1, 2, \ldots, N$, as shown in figure 16(*b*), it can be seen that a point is reached, say $n = N_0$, where the sums change sign from positive to negative. The collection of contributions for $n \geqslant N_0$ may be viewed as the reason why the correlation is negative, since the other contributions cancel out between plus and minus. The fraction of events that are responsible for the correlation, namely $(N - N_0)/N$, as well as the distribution of the magnitudes of the contributing subset of paths, reveals useful information about the origin of the Reynolds shear stress.

Figure 17 is a plot for each of the terms in (2.7) of the fraction of events (e.g. $(N - N_0)/N$ in the example corresponding to figure 16) at each y^+ position whose contribution is not cancelled by events with the opposite sign. It is seen in figure 17(*a*) that for a large portion of the channel, Φ_D and $\overline{uv}$ follow a very similar trend in which approximately 20 % of events are responsible for their occurrence. The percentage for each of these rises towards 30 % at $y^+ = 15$ and drops towards zero for small y^+. As y^+ approaches the centreline, $\overline{u_a v_a} \to 0$, as does the corresponding fraction of significant events shown in figure 17(*a*). The latter trend is due to the natural cancellation of plus and minus events that must take place as the centreline
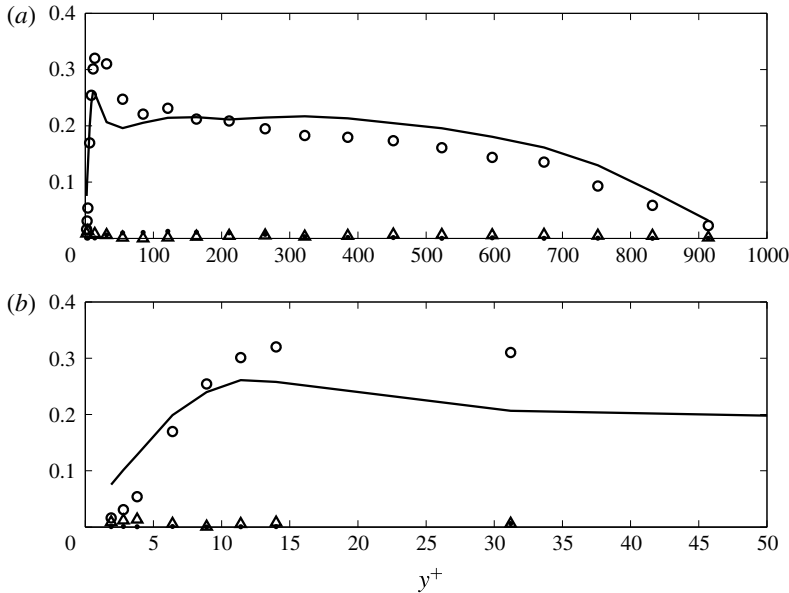
FIGURE 17. The fraction of points in the data ensembles that account for the local computed values of the terms in (2.7): ——, $\overline{u_a v_a}$; $\bigcirc$, Φ_D; $\triangle$, $(\Phi_A + \overline{u_b v_a})$; (*a*) whole channel; (*b*) detail of the near-wall region.

is reached in a symmetric flow field. In the near-wall region, as highlighted in figure 17(*b*), even though the Reynolds shear stress is rapidly dropping in magnitude towards zero at the wall from the peak it had at $y^+ = 40$, this has no bearing on the frequency of events contributing to Φ_D until very close to the wall, in fact, within $y^+ = 10$. This suggests that throughout the near-wall region, outside the viscous sublayer, the drop off in $\overline{u_a v_a}$ is not due to a decrease in the number of Reynolds stress producing events, but rather to the size of their contributions. Within the viscous sublayer itself, the frequency of Reynolds stress producing events diminishes, and with this $\overline{u_a v_a}$ becomes very small. In the same vein, it can be anticipated that the decrease in the magnitude of correlations such as Φ_D for $\tau > \tau_D$ can be attributed to a decrease in the number of events that maintain coherency with v_a as the elapsed time increases. At the same time, the relatively slow relaxation of Φ_D towards zero attests to the longevity of a small number of significant Reynolds stress producing events in the flow field.

The special importance of Φ_D to the Reynolds shear stress is indirectly implied by the fact that Φ_A and $\overline{u_b v_a}$ are non-zero only due to a comparatively small number of events in the flow field. Thus, in contrast to displacement transport, where it can be expected that at any time approximately one fifth of the domain contains sources of Reynolds stress correlation, the other terms are the result of an occasional somewhat rare event. In fact, for virtually the entire channel, considerably less than 1 % of events in the samples explain why Φ_A and $\overline{u_b v_a}$ are non-zero. The conclusion may be reached that besides being the dominant factor leading to Reynolds stress, the events causing Φ_D to be prominent must represent a far more common process throughout the flow field than that leading to Φ_A and $\overline{u_b v_a}$.
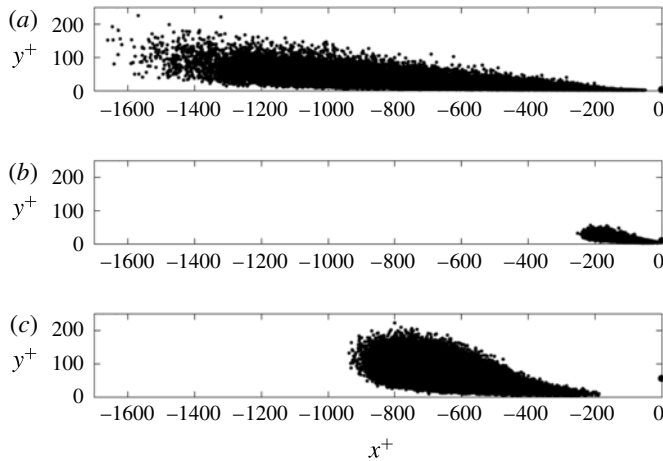
FIGURE 18. Side view in the x^+, y^+ plane scatter plot of upstream particle positions at $t^+ - \tau_D^+$ arriving at t^+: (a) $y^+ = 2.8$; (b) $y^+ = 8.9$; (c) $y^+ = 54.8$.

7. Upstream analysis

It is of some interest to consider the upstream statistics of fluid particles that travel over the time τ_D^+ to arrive at fixed y^+ planes. This kind of information is helpful for understanding the physics of transport and potentially for providing insights into accurately modelling the process. In this section, we consider the properties of all particles arriving at y^+ positions, while, in the next section, we look at statistics for the subset of paths that are most directly connected with the presence of the Reynolds shear stress.

Some basic attributes of the ensemble of particles that arrive at given y^+ locations at time t^+ can be gleaned from figures 18 and 19, containing scatter plots in the x^+, y^+ plane of where the particles were located at the earlier time $t^+ - \tau_D^+$. The first of these figures is for particles arriving at $y^+ = 2.8$, 8.9, 54.8 and the second is for $y^+ = 163$, 452, 832. The mixing times associated with these points are $\tau_D^+ = 86.5$, 12.7, 41.6, 154.0, 435.7, and 598.0 respectively. In each figure, the ending point of the particles is indicated by a circle at the $x^+ = 0$ position. The plots show that the streamwise extent of the particle ensembles is a strong function of the local mixing time. This explains the very short upstream region for the data at $y^+ = 8.9$, which is where the mixing time is at a minimum. The shapes of the scatter plots largely reflect the fact that particles travelling from closer to the wall are slower, so their starting points are closer to the streamwise end point. The particles arriving at $y^+ = 2.8$ are mostly travelling from further away from the wall so are arrayed beyond this point.

Figure 19 shows that particles travel from an increasingly distant upstream region that spreads outward rapidly as the terminal y^+ point increases. For the particles arriving at $y^+ = 452$ and 832, many have started from beyond the centreline. This creates the hooked appearance of the particles. In all cases, the ensemble of particles includes many that originate from close to the lower wall surface. It is interesting to observe that for the $y^+ = 832$ location, particles originate from the entire extent of the channel from one wall to the other.

The upstream locations plotted in figures 18 and 19 are based on timings of the maximum contributions to displacement transport, so that they are reflective of the most coherent motions of dynamical significance in the flow. Clearly, these figures
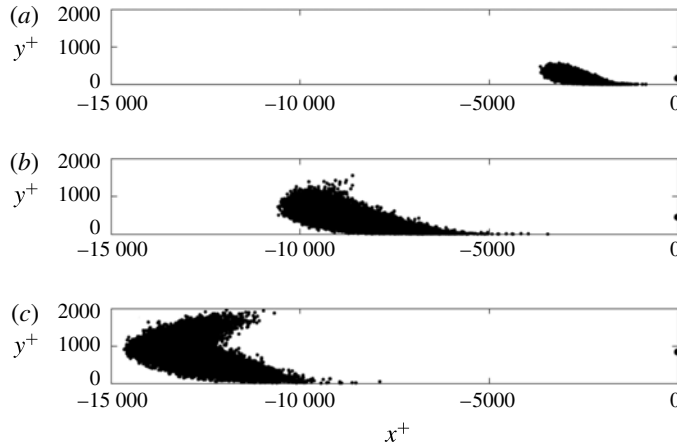
FIGURE 19. Side view in the x^+, y^+ plane scatter plot of upstream particle positions at $t^+ - \tau_D^+$ arriving at t^+: (*a*) $y^+ = 163$; (*b*) $y^+ = 452$; (*c*) $y^+ = 832$.

show that the Reynolds shear stress must ultimately be viewed as the result of actions covering a large region in space–time, particularly for the data in figure 19, where the particles travel thousands of x^+ units and several hundred t^+ units to make the maximum contribution to transport. According to the figure, the correlation between u_a and v_a at $y^+ = 832$ appears to have its origin in motions originating over five channel widths upstream. Even at $y^+ = 154$, the correlation arises from particles travelling more than a channel width upstream. From this perspective, there appears to be little that is local about the Reynolds shear stress.

The lateral spread of particles in the ensembles is shown in figure 20 for ending points on the planes $y^+ = 2.8$, 163 and 452. As expected, the distributions are symmetric in the spanwise direction. The shapes of the particle distributions reflect a bias towards the upstream direction, which is another indication of how the varying mean velocity differentially affects the motion of particles travelling from below versus above the final destination. Since the lateral motion of the particles can be viewed as the sum of many small steps, irrespective of their vertical positions in the channel, a Gaussian distribution in the initial path positions is not unexpected.

The Kolmogorov–Smirnov (KS) test was used to examine the goodness-of-fit hypothesis that the upstream spanwise particles obey a Gaussian distribution. The KS test is based on the maximum difference between an empirical and a hypothetical cumulative distribution function (Massey 1951). In the present case, a Gaussian distribution function was fitted to the initial z positions of the particles which was then compared with the data. It was found that the Gaussian hypothesis is met with a confidence interval of 99 % for all y^+ levels, suggesting that the distribution of transverse particle positions is indeed Gaussian. Figure 21 illustrates at four y^+ positions the degree to which the computed upstream initial z positions fit the form of a Gaussian cumulative distribution function.

The probability density functions in the x and y directions could not be reliably fitted to any common distributions. Nonetheless, it is informative to consider the mean of the x_b data as well as the standard deviations of the x_b, y_b, z_b data, as shown in figures 22(*a*) and 22(*b*) respectively. Apart from a small increase in the viscous sublayer, the mean of x_b decreases linearly with y^+ until approximately
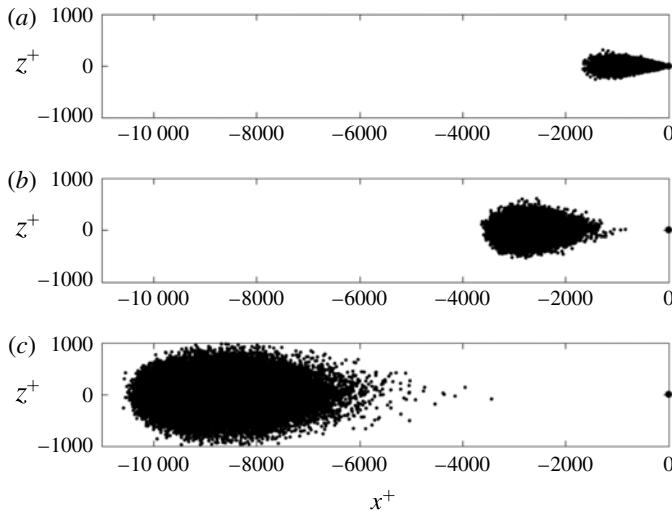
FIGURE 20. Top view in the x^+, z^+ plane of upstream positions at $t^+ - \tau_D^+$ of particles arriving at t^+ at (a) $y^+ = 2.8$, (b) $y^+ = 163$ and (c) $y^+ = 452$.
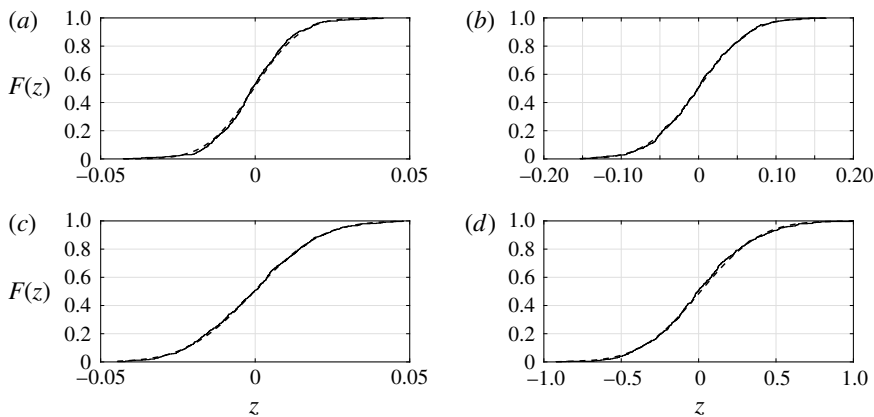

FIGURE 21. The cumulative distribution function (CDF) for upstream spanwise particle position (solid line) compared with the fitted Gaussian CDF (dashed line): (a) $y^+ = 8.9$; (b) $y^+ = 54.8$; (c) $y^+ = 211$; (d) $y^+ = 523$.

$y^+ = 600$, after which it is approximately constant at a value of the order of six channel widths upstream of the endpoint. The linear behaviour of the mean of x_b appears to be consistent with the linearity of τ_D^+ over the same range as seen in figure 7(a) and occurs despite the changes in mean velocity over this portion of the channel. Figure 22(b) shows that the standard deviation of the upstream particle locations in all three directions also increases somewhat linearly until $y^+ = 600$, after which the standard deviation is approximately constant in the wall-normal and spanwise directions and falls in the streamwise direction. The upstream dispersion of the particles is much larger in the streamwise direction than either of the other directions, with the latter becoming close to each other by the centreline. The decrease in standard deviation in the x direction in figure 22(b) shows that there is less of a
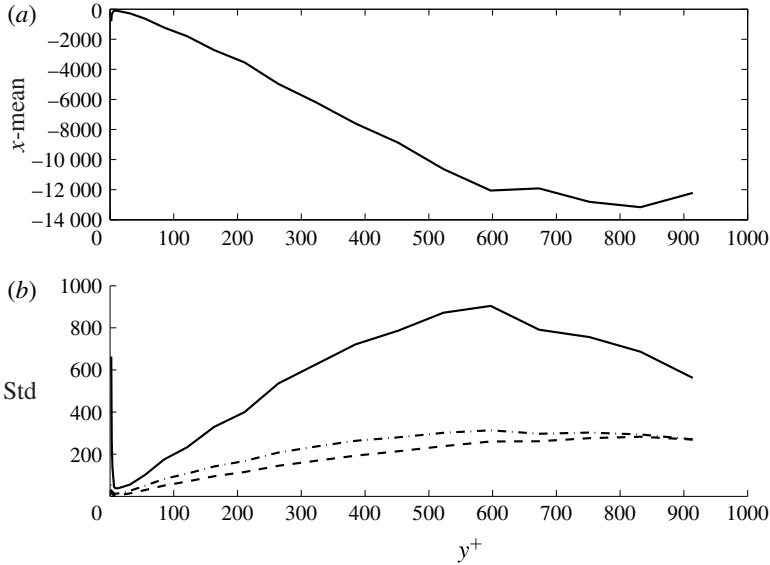
FIGURE 22. (*a*) The streamwise mean of particles arriving at y^+ planes over the mixing time τ_D. (*b*) The standard deviation of upstream particle locations: ——, x direction; – – –, y direction; — · —, z direction.

spread in initial x position far from the wall, suggesting a reduced role for the slower moving particles originating close to the wall. The statistics in figure 22 imply that all points within the central channel core beyond $y^+ = 600$ share a similar transport physics that reflects a reduced influence of the solid boundaries.

8. Modelling

To the extent that the decomposition in (2.7) is taken as a route towards developing a physical explanation for the Reynolds shear stress, then it is required to develop models for the phenomena described by the individual terms. In view of the previous discussions, it is clear that the most important facet of the Reynolds stress physics is that associated with the classical idea of displacement transport. Here, we will show using the channel flow path data accumulated in this study how a practical and self-consistent basis can be set up for evaluating displacement transport. Generalization of the approach to other flows should be possible. Less clear is how the small contribution to Reynolds stress from the remaining terms in (2.7) as shown in figure 10 may be modelled. Such an effort, not considered here, will require firming up of the connection between structural features of the flow and their influence on particle acceleration and the $\overline{u_b v_a}$ correlation.

To develop a model for $\overline{v_a(\overline{U}_b - \overline{U}_a)}$, it should be noted that this expression can be evaluated in the form of an ensemble average over N particle paths via

$$\overline{v_a(\overline{U}_b - \overline{U}_a)} = \frac{1}{N} \sum_{i=1}^{N} v_a^i (\overline{U}_b^i - \overline{U}_a), \tag{8.1}$$

where the superscript i denotes the particular member of the ensemble. In view of our previous discussion, in which the members of the ensemble are ordered from plus to

minus in magnitude, (8.1) can be written as

$$\overline{v_a(\overline{U}_b - \overline{U}_a)}(y) = \frac{1}{N}\left[\sum_{i=1}^{N_0} v_a^i(\overline{U}_b^i - \overline{U}_a) + \sum_{i=N_0+1}^{N} v_a^i(\overline{U}_b^i - \overline{U}_a)\right], \qquad (8.2)$$

where it is assumed that the first sum in this relation is over those contributions to the left-hand side that cancel out plus and minus, while the second sum contains those that are of one sign and together are responsible for the non-zero value of Φ_D. With this understanding, (8.2) can be written as

$$\overline{v_a(\overline{U}_b - \overline{U}_a)}(y) = \frac{1}{N}\left[\sum_{i=N_0+1}^{N} v_a^i(\overline{U}_b^i - \overline{U}_a)\right]. \qquad (8.3)$$

The $N - N_0$ terms that remain in (8.3) have initial points of travel in the wall-normal direction, namely y_b^i, that are either above or below y. Letting N_B be the number from below and N_T be the number from above, then $N_B + N_T = N - N_0$. The sum in (8.3) can now be divided into two separate sums of particles, one of which has $y_b^i < y$ and the other of which has $y_b^i > y$. This results in

$$\overline{v_a(\overline{U}_b - \overline{U}_a)}(y) = \frac{1}{N}\left[\left(\sum_{i=1}^{N_B} v_B^i(\overline{U}_b^i - \overline{U}_a)\right) + \left(\sum_{i=1}^{N_T} v_T^i(\overline{U}_b^i - \overline{U}_a)\right)\right], \qquad (8.4)$$

where now v_B^i and v_T^i respectively refer to the values of v_a^i for particles originating below and above y. It is also assumed here that the index i is reset to be $1 \leqslant i \leqslant N_B$ and $1 \leqslant i \leqslant N_T$ respectively for the two sets of particles. The two summations within parentheses on the right-hand side of (8.4) represent averages over the subensembles of points coming from below and above the destination point. The ratios N_B/N and N_T/N add up to the ratio $(N - N_0)/N$ that was discussed in §6 and plotted in figure 17.

Since $\overline{U}_b$ depends only on y, a simplification of (8.4) can be had by organizing the elements of each of the two subensembles of paths according to their values of y_b^i. For convenience, we refer to these y values as being in the ensembles y_B^i, $i = 1, \ldots, N_B$, and y_T^i, $i = 1, \ldots, N_T$. Figure 23 is a scatter plot of y_b^i, v_a^i values for the data at $y^+ = 211$ that is representative of all points in the channel. Points travelling from below the final point are seen to all arrive at the final plane with positive values of v_a and those travelling from above invariably have negative v_a values. Clearly, paths for which travel to or from the wall is uninterrupted over the mixing time are favoured in contributing to the Reynolds shear stress.

Now, we consider the set of particles coming from below the final plane. The upstream values lie between

$$y_B^{min} \equiv \min(y_B^i, i = 1, \ldots, N_B) \qquad (8.5)$$

and

$$y_B^{max} \equiv \max(y_B^i, i = 1, \ldots, N_B). \qquad (8.6)$$

We divide the region $y_B^{min} \leqslant y \leqslant y_B^{max}$ into K equal subdivisions of length $\Delta y'$, with y_k' being the centre of the kth box. Let N_B^k be the number of particles for which y_b^i is
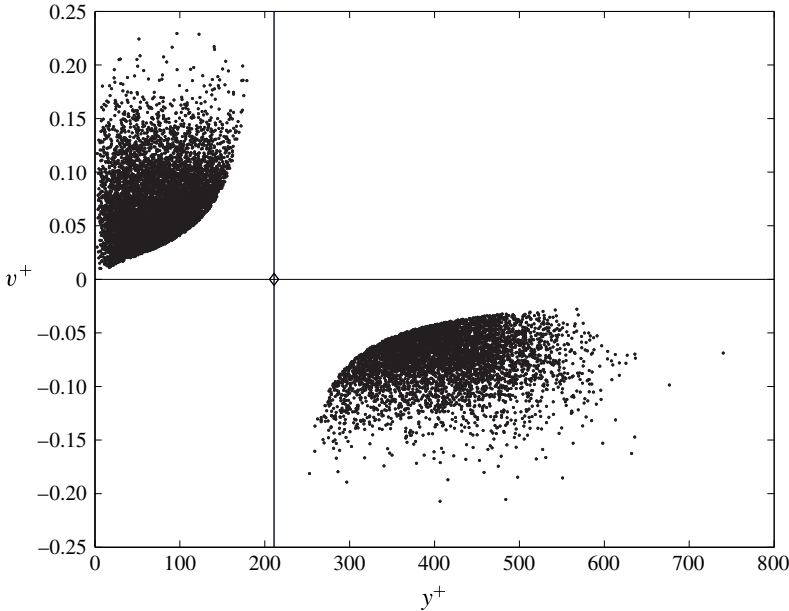
FIGURE 23. Scatter plot of y_b, v_a values for particles from the subensembles of significant contributors to $\overline{uv}$ arriving at $y^+ = 211$.

in the kth box and let $p_B^k = N_B^k/N_B$ be the fraction of the N_B particles initiating in the kth subdivision where $\sum_k N_B^k = N_B$. We define

$$c_B^k = p_B^k/\Delta y' \tag{8.7}$$

as the concentration of particles in the kth box. Let $\overline{v}_B^k$ be the average of the v_b^i velocities in the kth box. Using these definitions, the first term on the right-hand side of (8.4) becomes

$$\frac{1}{N} \sum_{i=1}^{N_B} v_B^i (\overline{U}_b^i - \overline{U}_a) = \frac{1}{N} \sum_{k=1}^{K} \left(\sum_{i=1}^{N_B^k} v_B^i (\overline{U}(y_k') - \overline{U}(y)) \right)$$

$$= \frac{1}{N} \sum_{k=1}^{K} N_B^k \overline{v}_B^k (\overline{U}(y_k') - \overline{U}(y))$$

$$= \frac{N_B}{N} \sum_{k=1}^{K} c_B^k \overline{v}_B^k (\overline{U}(y_k') - \overline{U}(y)) \Delta y'. \tag{8.8}$$

The relative importance of N_B/N and N_T/N divides the result in figure 17 into fractions from above and below that change with y. Then, we define

$$\alpha_B(y) = \frac{N_B}{N}, \quad \alpha_T(y) = \frac{N_T}{N}. \tag{8.9a,b}$$

Using (8.9) in the last expression of (8.8) and taking the limit as $\Delta y' \to 0$, we obtain the integral

$$\alpha_B(y) \int c_B(y, y') \overline{v}_B(y, y') (\overline{U}(y') - \overline{U}(y)) \, \mathrm{d}y', \tag{8.10}$$

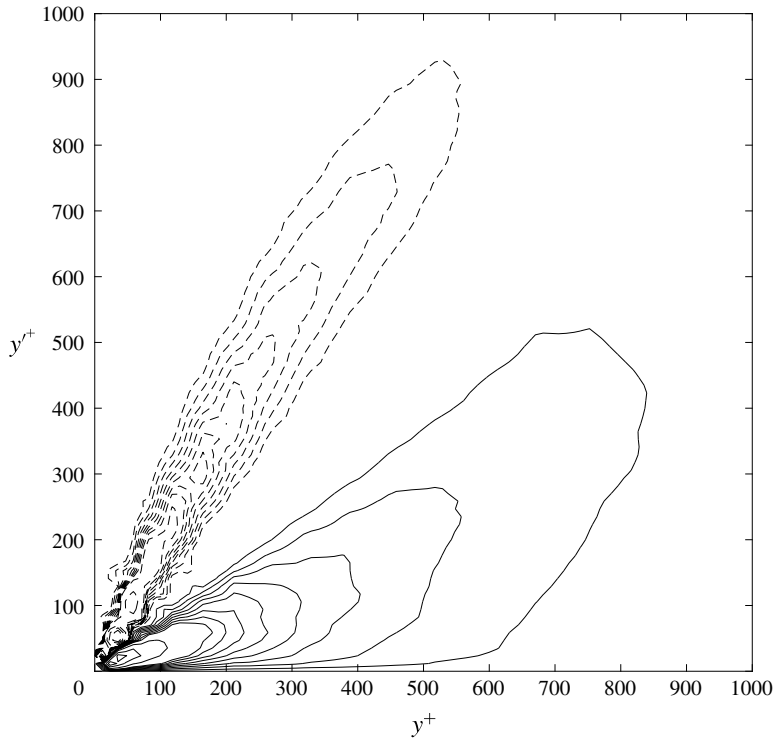where the integration limit is from one wall of the channel to the other.

FIGURE 24. Contour plot of $F(y^+, y'^+)$ in the lower half channel. Solid lines are positive values and dashed lines are negative values.

Use of a similar analysis of the contributions to the displacement transport term coming from particles originating above the destination plane leads to an expression equivalent to (8.10) and containing $\alpha_T(y)$, $\overline{v}_T(y, y')$ and $c_T(y, y')$. From these results, the derived model for the displacement transport term is

$$\overline{v_a(\overline{U}_b - \overline{U}_a)} = \int_0^h F(y, y')(\overline{U}(y') - \overline{U}(y))\, \mathrm{d}y', \tag{8.11}$$

where the kernel function is

$$F(y, y') = \alpha_B(y)c_B(y, y')\overline{v}_B(y, y') + \alpha_T(y)c_T(y, y')\overline{v}_T(y, y'). \tag{8.12}$$

At any given y location in the channel, (8.11) shows how the displacement transport term arises from fluid particles travelling from different y' positions. This relation takes advantage of the streamwise uniformity in channel flow to develop a compact formula. In more general situations, it can be expected that the potentially significant upstream origin of the particles arriving at destination points would have to be taken into account in deriving formulae similar to (8.12).

The most essential part of the physics behind the Reynolds shear stress is contained in the function $F(y, y')$. To determine it numerically, its values on the 23 y^+ locations where particle data were obtained were computed and then these values were interpolated into a square mesh covering the lower half channel. A numerical calculation shows that the computed $F(y, y')$ is fully self-consistent with (8.11).
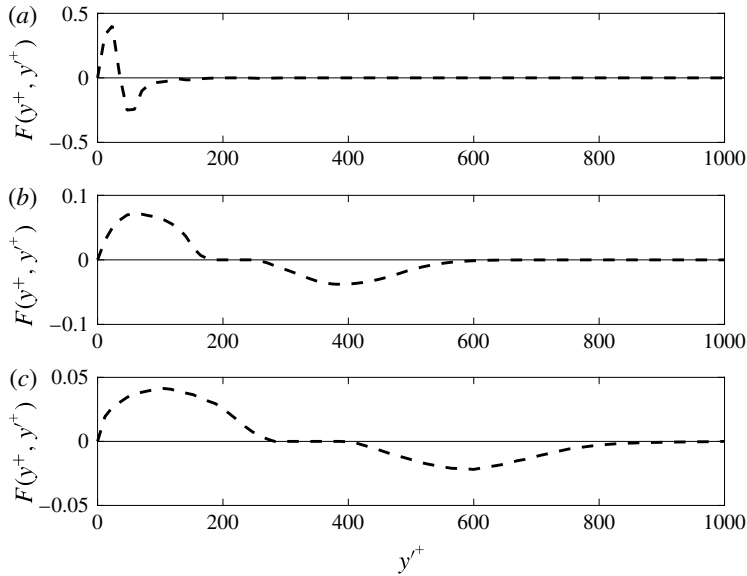
FIGURE 25. Plot of $F(y^+, y'^+)$ for the y^+ values (*a*) 35.3, (*b*) 211.7 and (*c*) 329.2.

A holistic view of $F(y^+, y'^+)$ for the lower channel half is shown in figure 24, which puts into sharp focus the intrinsic non-locality of the mechanism responsible for the Reynolds shear stress. Taken as a whole, figure 24 calls into question the relevance of the local mean velocity derivative in determining displacement transport.

Near the wall, the peak contributions to the local displacement transport at a particular point come from fluid particles that originate at points offset immediately to either side of the point in question. The peaks move apart with increasing distance from the wall, creating a growing separation between the influences of particles travelling from below and above the destination point. Figure 25 is a plot of the y'^+ dependence of $F(y^+, y'^+)$ at the three locations $y^+ = 35.3$, 211.7 and 329.2. The plots show how the peak positive contributions rapidly decrease in magnitude with distance from the wall, reflecting the spreading out of the region of influence on Φ_D of initial particle locations. The increasing extent of the region centred on each y^+ location from which particles contributing to displacement transport do not originate is apparent. According to figure 24, such a region first develops at $y^+ \approx 100$ and increases significantly with distance from the wall. This trend appears to call into question the appropriateness of a local dependence of the Reynolds shear stress on the mean velocity gradient, even in the region away from the wall seen in figure 15 where a gradient model seems to be justified. However, there is an implicit dependence of Φ_D on the mean gradient over the mixing time in the difference between mean velocities in (8.11). This is made particularly clear in the case of homogeneous shear flow, where (5.10) applies. For channel flow and presumably for flows encountered in engineering practice, the implication of (8.11) is that gradient transport is not an appropriate means of accounting for the full effect of displacement transport.

9. Conclusions

This study has aimed at illuminating some of the principal physical processes leading to the transport of momentum as represented by the Reynolds shear stress in

a channel flow. Expanding on a much-limited previous study in which the near-wall region of a low-Reynolds-number channel flow was analysed, here, an investigation is made of a channel flow at much higher Reynolds number via ensembles of backward fluid particle paths collected at many locations across the flow field. The Lagrangian decomposition of $\overline{uv}$ showed that the classical displacement transport effect accounts for most of the correlation. Acceleration transport effects as well as the somewhat specialized influence of near-wall structures in extending the correlation in $\overline{u_b v_a}$ provide a non-negligible local contribution to $\overline{uv}$ near its peak amplitude. Besides the relative sizes of the different physical processes affecting transport, the displacement transport effect is found to result from the consistent action of a sizable fraction – approximately 20 % – of the flow field at any given time, while the remaining contributions are the result of somewhat rare isolated events.

The transport analysis is built on a mixing time associated with the peak correlation between the change in mean momentum along fluid particle paths and the normal velocity at the destination point. For much of the channel, the space/time location where this correlation is greatest lies much earlier in time at distances far upstream, as far as six channel widths. Only in the buffer layer where turbulence intensities are strongest is the maximum upstream contribution to displacement transport within a short upstream distance, in fact as near as 1/10 of a channel width.

A non-local model for displacement transport was derived whose kernel function was numerically evaluated using the particle path data sets. Due to the symmetries of channel flow, the model captures the essential causes of the displacement transport in a compact form involving only distance across the channel. In more general settings, it can be anticipated that two- and three-dimensional kernel functions would be required to capture the transport physics. For turbulent channel flow, and presumably many other shear flows, the analysis gives little support to the idea that a mean gradient model is an appropriate means of representing the physics of the Reynolds shear stress.

Acknowledgements

REFERENCES

ARAYA, G. & CASTILLO, L. 2012 DNS of turbulent thermal boundary layers up to $Re_\theta = 2300$. *Intl J. Heat Mass Transfer* **55**, 4003–4019.

BERNARD, P. S. 2013 Vortex dynamics in transitional and turbulent boundary layers. *AIAA J.* **51**, 1828–1842.

BERNARD, P. S. & HANDLER, R. A. 1990 Reynolds stress and the physics of turbulent momentum transport. *J. Fluid Mech.* **220**, 99–124.

BERNARD, P. S., THOMAS, J. M. & HANDLER, R. A. 1993 Vortex dynamics and the production of Reynolds stress. *J. Fluid Mech.* **253**, 385–419.

BERNARD, P. S. & WALLACE, J. M. 2002 *Turbulent Flow: Analysis, Measurement and Prediction*. Wiley.

BOUDJEMADI, R., MAUPU, V., LAURENCE, D. & QUR, P. L. 1997 Budgets of turbulent stresses and fluxes in a vertical slot natural convection flow at Rayleigh $Ra = 10^5$ and 5.4 10^5. *Intl J. Heat Fluid Flow* **18**, 70–79.

CORRSIN, S. 1974 Limitations of gradient transport models in random walks and turbulence. *Adv. Geophys.* **18A**, 25–60.

DIMITROPOULOS, C. D., SURESHKUMAR, R., BERIS, A. N. & HANDLER, R. A. 2001 Budgets of Reynolds stress, kinetic energy and streamwise enstrophy in viscoelastic turbulent channel flow. *Phys. Fluids* **13**, 1016–1027.

EGOLF, P. W. 1994 Difference-quotient turbulence model: a generalization of Prandtl's mixing-length theory. *Phys. Rev.* E **49**, 1260–1268.

EGOLF, P. W. 2009 Lévy statistics and beta model: a new solution of 'wall' turbulence with a critical phenomenon. *Intl J. Refrig.* **32**, 1815–1836.

EGOLF, P. W. & WEISS, D. A. 1998 Difference-quotient turbulence model: the axisymmetric isothermal jet. *Phys. Rev.* E **58**, 459–469.

GATSKI, T. B. & SPEZIALE, C. G. 1993 On explicit algebraic stress models for complex turbulent flows. *J. Fluid Mech.* **254**, 59–78.

GRAHAM, J., KANOV, K., YANG, X. I. A., LEE, M., MALAYA, N., LALESCU, C. C., BURNS, R., EYINK, G., SZALAY, A., MOSER, R. D. & MENEVEAU, C. 2016 A web services accessible database of turbulent channel flow and its use for testing a new integral wall model for LES. *J. Turbul.* **17**, 181–215.

HAMBA, F. 2005 Nonlocal analysis of the Reynolds stress in turbulent shear flow. *Phys. Fluids* **17**, 115102.

HAMBA, F. 2013 Exact transport equation for local eddy viscosity in turbulent shear flow. *Phys. Fluids* **25**, 085102.

HANDLER, R. A., BERNARD, P. S., ROVELSTAD, A. & SWEARINGEN, J. 1992 On the role of accelerating particles in the generation of Reynolds stress. *Phys. Fluids* A **4**, 1317–1319.

JONES, W. P. & LAUNDER, B. E. 1972 The prediction of laminarization with a two-equation model of turbulence. *Intl J. Heat Mass Transfer* **15**, 301–314.

KAYS, W. M. & CRAWFORD, M. E. 1993 *Convective Heat and Mass Transfer*, 3rd edn. McGraw-Hill.

LESIEUR, M. & MÉTAIS, O. 1996 New trends in large-eddy simulations of turbulence. *Annu. Rev. Fluid Mech.* **28**, 45–82.

LI, Y., PERLMAN, E., WAN, M., YANG, Y., MENEVEAU, C., BURNS, R., CHEN, S., SZALAY, A. & EYINK, G. 2008 A public turbulence database cluster and applications to study Lagrangian evolution of velocity increments in turbulence. *J. Turbul.* **9**, 1–29.

MANSOUR, N. N., KIM, J. & MOIN, P. 1988 Reynolds-stress and dissipation-rate budgets in a turbulent channel flow. *J. Fluid Mech.* **194**, 15–44.

MASSEY, F. J. 1951 The Kolmogorov–Smirnov test for goodness of fit. *J. Am. Stat. Assoc.* **46**, 68–78.

MENTER, F. R. 1994 Two-equation eddy-viscosity turbulence models for engineering applications. *AIAA J.* **8**, 1598–1605.

PERLMAN, E., BURNS, R., LI, Y. & MENEVEAU, C. 2007 Data exploration of turbulence simulations using a database cluster. In *Proceedings of the 2007 ACM/IEEE Conference on Supercomputing*, pp. 1–11. ACM.

PERRY, A. E. & CHONG, M. S. 1982 On the mechanism of wall turbulence. *J. Fluid Mech.* **119**, 173–217.

PRANDTL, L. 1925 Bericht über Untersuchungen zur ausgebildeten Turbulenz. *Z. Angew. Math. Mech.* **5**, 136–139.

PRANDTL, L. 1942 Bemerkungen zur Theorie der freien Turbulenz. *Z. Angew. Math. Mech.* **22**, 241–243.

SAGAUT, P. 2006 *Large Eddy Simulation for Incompressible Flows*, 3rd edn. Springer.

SCHMITT, F. G. 2007 About Boussinesq's turbulent viscosity hypothesis: historical remarks and a direct evaluation of its validity. *C. R. Mécanique* **335**, 617–627.

SPALART, P. R. & ALLMARAS, S. R. 1994 A one-equation turbulence model for aerodynamic flows. *Rech. Aerosp.* **1**, 5–21.

SPEZIALE, C. G. 1987 On nonlinear k–l and k–ϵ models of turbulence. *J. Fluid Mech.* **178**, 459–475.

TAYLOR, G. I. 1932 The transport of vorticity and heat through fluids in turbulent motion. *Proc. R. Soc. Lond.* A **135**, 685–705.

TOSCHI, F. & BODENSCHATZ, E. 2009 Lagrangian properties of particles in turbulence. *Annu. Rev. Fluid Mech.* **41**, 375–404.

WILCOX, D. C. 2008 Formulation of the k–ω turbulence model revisited. *AIAA J.* **46**, 2823–2838.

WU, X. & MOIN, P. 2009 Direct numerical simulation of turbulence in a nominally zero-pressure-gradient flat-plate boundary layer. *J. Fluid. Mech.* **630**, 5–41.

YOSHIZAWA, A. 1984 Statistical analysis of the deviation of the Reynolds stress from its eddy-viscosity representation. *Phys. Fluids* **27**, 1377–1387.